IEEE Access
Multidisciplinary : Rapid Review : Open Access Journal

Received May 22, 2020, accepted June 8, 2020, date of publication June 11, 2020, date of current version June 24, 2020.

Digital Object Identifier 10.1109/ACCESS.2020.3001852

Blind Calibration of Phase Drift in Millimeter-Wave Channel Sounders

JACK CHUANG[1], JELENA SENIC[1], CHUNMEI LIU[1], CAMILLO GENTILE[1], (Member, IEEE), SUNG YUN JUN[2], (Member, IEEE), AND DEREK CAUDILL[2]

[1]Wireless Networks Division, National Institute of Standards and Technology, Gaithersburg, MD 20899, USA
[2]RF Technology Division, National Institute of Standards and Technology, Boulder, CO 80305, USA

Corresponding author: Camillo Gentile (camillo.gentile@nist.gov)

This work was supported by United States government.

ABSTRACT Millimeter-wave channel sounders are much more sensitive to phase drift than their microwave counterparts by virtue of shorter wavelength. This matters when coherently combining untethered channel measurements – scanned over multiple antennas either electronically or mechanically in seconds, minutes, or even hours – to obtain directional information. To eliminate phase drift, a synchronization cable between the transmitter and receiver is required, limiting deployment range and flexibility indoors, and precluding most outdoor and mobile scenarios. Instead, we propose a *blind* technique to calibrate for phase drift by post-processing the channel measurements; the technique is referred to as blind because it requires no reference signal and, as such, works even in non-line-of-sight conditions when the (reference) direct path goes undetected. To substantiate the technique, it was tested on real measurements collected with our 60 GHz virtual phased-array channel sounder, as well as through simulation. The technique was demonstrated robust enough to deal with the most severe case of phase drift (uniformly distributed phase) and in non-line-of-sight conditions.

INDEX TERMS 5G, beamforming, clock drift, mmWave, phased-array antennas, phase coherence.

I. INTRODUCTION

The design and deployment of fifth-generation (5G) communication networks, based on millimeter-wave (mmWave) technology, are currently underway. The transition from 4G was prompted by the availability of large swaths of mmWave spectrum to alleviate the saturated sub-6 GHz band, enabling instantaneous transmission bandwidths in excess of 1 GHz and in turn speeds 100 times faster. Although networks have witnessed generational transitions in the past, this one is more pronounced due to the quantum leap in the frequency of operation, to 28 GHz and beyond. Higher operating frequency, however, carries with it the burden of greater path loss (free-space loss, penetration loss, and oxygen-absorption loss at 60 GHz), which will be compensated through high-gain antennas. Because antenna beamwidth is inversely proportional to gain, beams will be only several degrees wide – a.k.a. *pencilbeams* – and consequently must be steered in the direction of ambient multipath to ensure adequate reception. The implication on mmWave channel sounders is that they too must incorporate directional antennas in order to develop appropriate channel models reduced from directional channel measurements.

Reference [1] provides a comprehensive review of mmWave channel sounders currently in use. The most popular systems feature a horn antenna that is mechanically rotated in azimuth and elevation, creating a virtual array of elements from the steering directions [2]–[10]. Another virtual architecture (such as the one implemented in this paper) also features a single antenna, however that is translated (not rotated) mechanically to positions half-wavelength apart, forming a phased-array antenna [11]–[13]. While virtual arrays have flexible inter-element spacing and are immune to mutual coupling, the mechanical movement implies scan durations on the order of minutes or even hours – much longer than the channel coherence time (the time over which the channel can be considered static) – and so are suitable for sounding static environments only. Millimeter-wave channel sounders that can deal with dynamic channels either feature a real array of horns that are switched electronically [14]–[16] or a real phased-array antenna that electronically steers beams [17]–[21]. They nevertheless can take up to seconds or even minutes for a complete angular scan depending on the angular resolution and scan range, whether the scan is

The associate editor coordinating the review of this manuscript and approving it for publication was Wei Fan.

spherical (in azimuth and elevation), and whether the scan is *double-directional* [22] (both at the transmitter (T) and receiver (R)).

A major research thrust in mmWave channel sounding is to obtain the best angular resolution possible. Super-resolution techniques such as CLEAN [23], MUSIC [24], ESPRIT [25], SAGE [26], RiMAX [27] (to name a few) can obtain angular resolution beyond the inherent beamwidth of the antennas, but require phase coherence across the array elements. While phase drift can be tolerated and somewhat mitigated at microwave to achieve reasonable accuracy [28]–[30], even the best Rubidium (Rb) clocks (which are state-of-the-art for synchronization between the T and R) have short-term clock drift rate of 1-2 ns/min [31], tantamount to phase drift of more than one cycle at 60 GHz for a scan duration just 1 s. The phase drift is exacerbated at mmWave due to much longer scan durations resulting from larger array sizes (or equivalent narrower beams), typically a few elements at microwave but easily in the hundreds at mmWave in order to synthesize high gain [32]. Even for shorter durations, spikes up to 4 ns in clock drift have been observed from non-fluid motion when one end of the sounder is mobile [31].

To eliminate phase drift, an optical cable is typically used for synchronizing the T and R [11]–[13], [33], however limiting flexibility and the maximum deployment distance indoors, and precluding most outdoor (due to damage from pedestrian and vehicular traffic) and mobile scenarios. Although some systems integrate GPS-disciplined Rb clocks with enhanced stability [15] to maintain gross timing (as do [9], [20], [31], [34] with free-running Rb), the stability is still orders of magnitude insufficient for phase coherence at mmWave. Even when an optical cable is employed, antenna arrays will still be subject to hardware tolerances (positional error in phase centers, mutual coupling between elements, mechanical stress, cable bending, etc.), phase noise, and temperature variation [12]. As such, techniques to calibrate for the consequential gain and phase biases between elements for microwave operation date back to the 1980s: Some calibration techniques are based on ground-truth reference signals whose angles, noise statistics, etc. are known [35]–[37]. Some *blind* calibration techniques forego a reference signal, but can resolve angle only to within an arbitrary rotational offset [38], [39]. Other blind techniques seek to optimize a non-convex objective, hence hinge upon a good initial calibration or can otherwise get trapped in a local minimum [40]–[46].

Although the aforementioned calibration techniques were designed for microwave operation (where the phase bias is typically small due to the relatively large wavelength), they have renewed interest today for mmWave antenna arrays. To our knowledge, none of these techniques have been applied to compensate for phase bias that originates from clock drift, the problem we address in this paper. In our application, the direct path (whose angle is given from the geometry of the T and R locations) can be used as a reference signal for non-blind techniques in line-of-sight (LoS) conditions, but it will generally go undetected in obstructed LoS (OLoS) or non LoS (NLoS) conditions due to high penetration loss at mmWave. Otherwise, a good initial calibration for blind techniques cannot be assumed since the drift is time-varying and can be as severe as uniformly distributed (shown later), depending on the scan duration; and tracking the drift from a known zero-state value is difficult due to the spiky nature of drift [31]. Finally, many of the blind techniques mentioned necessitate inverting matrices the size of the array, an operation that may be prohibitively expensive with array sizes in the hundreds (compared to just a few elements at microwave).

In light of this, in our paper we propose a blind calibration technique for phase drift in mmWave channel sounders that also mitigates against hardware tolerances, phase noise, and temperature variation. The proposed technique was verified against severe phase drift, through real measurements with our 60 GHz virtual phased-array channel sounder in NLoS conditions and over a scan duration of an hour, as well as through simulations with the worst case of phase drift (uniformly distributed) and in low signal-to-noise ratio (SNR) conditions. The remainder of this paper is developed as follows: Section II presents the proposed calibration technique and Section III describes our channel sounder. Verification of the proposed technique is conducted in Section IV and the final section is reserved for conclusions.

II. PHASE CALIBRATION TECHNIQUE

The technique to calibrate for phase drift is proposed in this section. The algorithm is preceded in the first subsection by a description of the channel impulse response, the data measured by channel sounders.

A. CHANNEL IMPULSE RESPONSE

Channel sounders measure the channel impulse response (CIR) between a pair of T and R antennas by transmitting a pulse defined in the delay domain (or in the frequency-domain equivalent) and sampling the complex amplitude of the received signal, $x(\tau)$. The received signal will appear as multiple copies of the transmitted pulse distorted by the channel, each corresponding to a discrete propagation path originating from transmission, reflection, diffraction, or refraction in the environment. So long as R is in the far field[1] of T and any scatterer in the environment, path k can be represented as a plane wave characterized through the following properties:

- delay τ_k, or time elapsed in propagation of the path from T to R;
- complex amplitude $a_k e^{j\phi_k}$, quantifying propagation loss (a_k) and any phase shift (ϕ_k) due to reflection or refraction;
- angle-of-departure (AoD) $\boldsymbol{\theta}_k^T = [\theta_k^{T,A} \theta_k^{T,E}]$ (from T) and angle-of-arrival (AoA) $\boldsymbol{\theta}_k^R = [\theta_k^{R,A} \theta_k^{R,E}]$ (to R), in both azimuth (A) and elevation (E) planes.

[1]The far field is typically defined as 10-20 wavelengths, e.g. > 10 cm at 60 GHz.

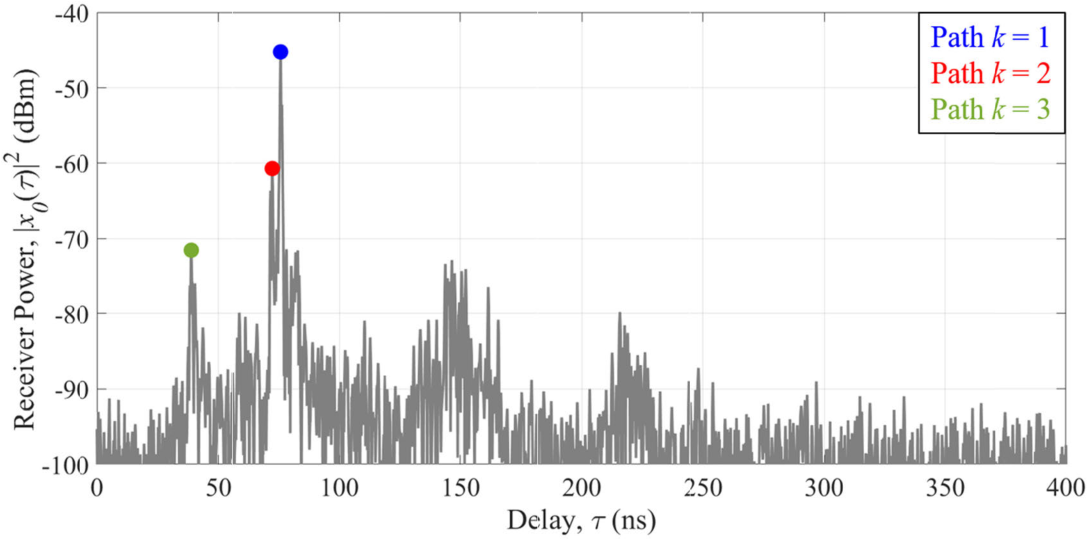

FIGURE 1. Channel impulse response, $x_0(\tau)$, measured at the first element of our virtual receiver array antenna. Highlighted are three illustrative paths that were clearly detected across all 900 elements.

For convenience, we denote double-directional angle as $\boldsymbol{\theta}_k = \left[\boldsymbol{\theta}_k^T \boldsymbol{\theta}_k^R\right]$.

CIRs are recorded between all element pairs of the T and R antenna arrays. Fig. 1 shows a CIR recorded at the first element, $x_0(\tau)$, of our channel sounder with a virtual phased-array antenna with 900 elements at the receiver. Although the same paths are detected across all elements, the paths have different amplitude, phase, and delay: The delay and amplitude are referred to as *large-scale* channel properties because they vary slowly across the array, given the relatively short displacement between elements[2] (typically a few to tens of millimeters) compared to the T-R distance (typically tens to hundreds of meters) and so can be considered constant, whereas phase is referred to as a *small-scale* channel property because it changes rapidly between elements by virtue of extremely short wavelength. As such, the phase is very sensitive to any bias resulting from hardware tolerances or clock drift.

Let the T array have N^T elements with known directional antenna gains and a steering vector defined by the $N^T \times 1$ vectors $\boldsymbol{g}^T\left(\boldsymbol{\theta}^T\right)$ and $\boldsymbol{s}^T\left(\boldsymbol{\theta}^T\right)$, respectively, in T's coordinate system, $\boldsymbol{\theta}^T$. The antenna gains are typically characterized in spherical space (azimuth and elevation) through far-field measurements in an anechoic chamber while the steering vector is a function of the antenna geometry (displacement or equivalent phase difference between element phase centers) and is typically characterized through laser inferometry [31]. Let the R array have analogous values of N^R, $\boldsymbol{g}^R\left(\boldsymbol{\theta}^R\right)$, $\boldsymbol{s}^R\left(\boldsymbol{\theta}^R\right)$, and $\boldsymbol{\theta}^R$. Now, let $\boldsymbol{x}(\tau)$ denote the $N^T N^R \times 1$ vector of measured CIRs between all T-R element pairs. A peak detector is applied to the CIRs to identify discrete paths across the delay samples. Then the signal vector corresponding to the k^{th} path arriving at sample delay bin τ_k is

$$\boldsymbol{x}(\tau_k) = a_k e^{j\phi_k} \cdot \boldsymbol{g}(\boldsymbol{\theta}_k) \odot \boldsymbol{s}(\boldsymbol{\theta}_k) \odot e^{j\boldsymbol{\delta}} + \boldsymbol{n}(\tau_k), \qquad (1)$$

defined by the following vectors of the same size: $\boldsymbol{g}(\boldsymbol{\theta}) = \text{vec}[\boldsymbol{g}^T\left(\boldsymbol{\theta}^T\right) \cdot \boldsymbol{g}^R\left(\boldsymbol{\theta}^R\right)^t]$ and $\boldsymbol{s}(\boldsymbol{\theta}) = \text{vec}[\boldsymbol{s}^T\left(\boldsymbol{\theta}^T\right) \cdot \boldsymbol{s}^R\left(\boldsymbol{\theta}^R\right)^t]$ are the respective double-directional antenna gains and steering vector (t denotes the transpose and $\boldsymbol{s}(\boldsymbol{\theta})$ is normalized such that $\angle s_0(\boldsymbol{\theta}) = 0$ without loss of generality), $\boldsymbol{\delta}$ is the phase drift, and $\boldsymbol{n}(\tau_k)$ is the sample noise.

The underlying assumption in (1), critical to the proposed calibration technique, is that all paths will suffer from the same phase drift. We maintain this to be perfectly reasonable because even though paths arrive at different delays, the delay between them is typically on the order of nanoseconds, for which any clock drift will be negligible: Consider a worse-case scenario for which the relative delay between paths is 333 μs, equivalent to a relative path length of 100 km, two orders of magnitude longer than what is the expected range for mmWave systems. The said relative delay for a Rb clock with a nominal drift of 1 ns/min is equivalent to just 0.002° in phase drift, three orders of magnitude less than the phase noise of any real system.

Another assumption implicit to (1) is that each delay sample will contain only one path, *i.e.* there are no overlapping pulses in the CIRs. The latter may be reasonable if the system has very high delay resolution – as do most mmWave channel sounders, typically with at least 1 ns delay resolution, or equivalent 1 GHz bandwidth – but this cannot be guaranteed; therefore a pruning step is necessary to identify $K \geq 2$ *distinct* (non-overlapping) paths. Details are left for the subsequent section, in which aspects of practical implementation are considered, using our channel sounder as an example.

[2]Even rotating virtual arrays may have displacement between elements due to the finite distance between the antenna phase center and the axis of rotation [10].

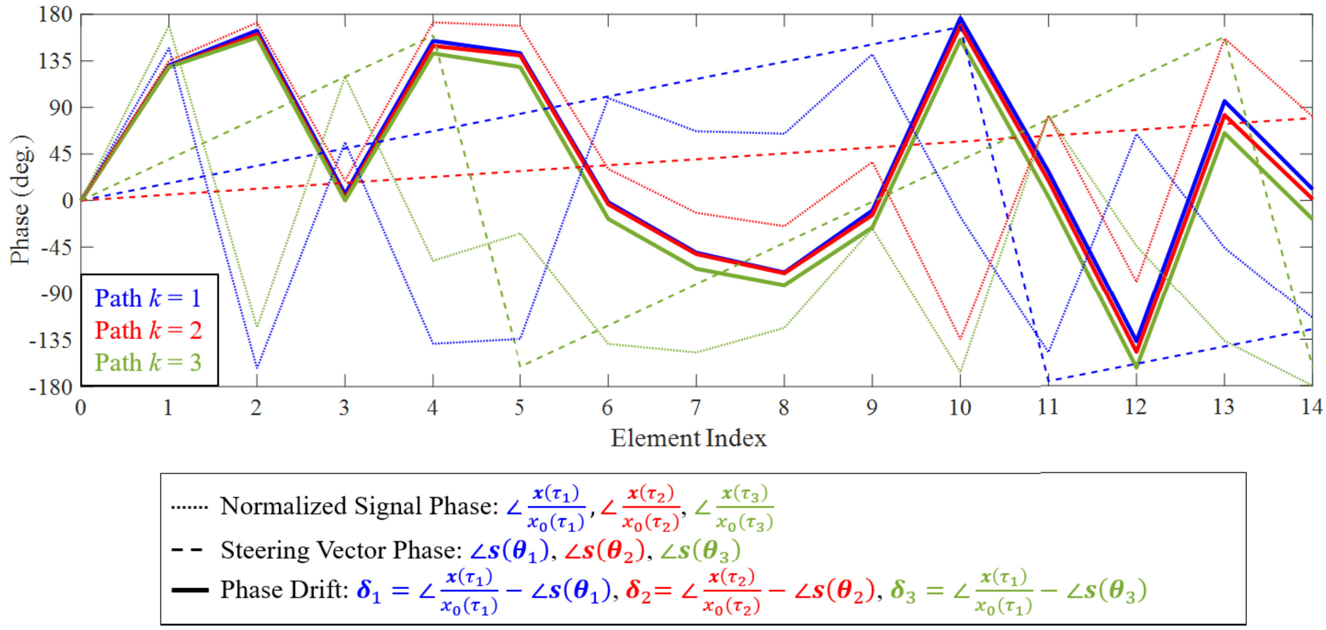

FIGURE 2. Phase drift across the first 15 elements of our virtual array, for the three distinct paths ($k = 1, 2, 3$) highlighted in the channel impulse response in Fig. 1.

B. ALGORITHM

The phase of signal k can be written from (1) as:

$$\angle \boldsymbol{x}(\tau_k) = \phi_k + \angle \boldsymbol{s}(\boldsymbol{\theta}_k) + \boldsymbol{\delta}_k, \tag{2}$$

where the phase noise from $\boldsymbol{n}(\tau_k)$ is absorbed in $\boldsymbol{\delta}_k$ (substituting for $\boldsymbol{\delta}$). It follows that with zero drift ($\boldsymbol{\delta}_k = \boldsymbol{0}$), the phase of $\boldsymbol{x}(\tau_k)$ is predicted from the phase of steering vector $\boldsymbol{s}(\boldsymbol{\theta}_k)$ (offset by the channel phase shift ϕ_k). Conversely, any non-zero drift will account for the difference between the signal phase and the steering vector phase. Accordingly, the drift can be estimated from the signal and the steering vector by rearranging (2) as $\boldsymbol{\delta}_k = \angle\frac{\boldsymbol{x}(\tau_k)}{x_0(\tau_k)} - \angle \boldsymbol{s}(\boldsymbol{\theta}_k)$; the normalization by $x_0(\tau_k)$ is introduced to cancel out ϕ_k, rendering the drift path-independent to within the phase noise (the normalization also sets $\delta_{k,0} = 0$ without loss of generality). In fact, Fig. 2 shows $\boldsymbol{\delta}_k$ (together with $\angle\frac{\boldsymbol{x}(\tau_k)}{x_0(\tau_k)}$ and $\angle \boldsymbol{s}(\boldsymbol{\theta}_k)$ used to compute it) across the first 15 elements of our virtual array for three distinct paths ($k = 1, 2, 3$) highlighted in the CIR in Fig. 1. Despite the stability of the Rb clocks, it can be observed that the drift at mmWave is large, even between adjacent elements. In fact, the drift between elements – collected only 4 s apart – was measured up to 180° (the worst possible case). Thankfully, the measured drift was approximately equal (to within the phase noise) between paths, the key to the proposed technique.

Now if $\boldsymbol{\theta}_k$ were known, the true drift $\boldsymbol{\delta}$ could simply be estimated by averaging over $\boldsymbol{\delta}_k$ (to suppress the noise); but in blind calibration, $\boldsymbol{\theta}_k$ is assumed to be unknown (nor can it be estimated given the large drift). So the first step in the calibration technique is to search a set of hypothesized angles $\tilde{\boldsymbol{\theta}}_k$ on a regularly spaced grid and, for each gridpoint, compute the corresponding drift:

$$\tilde{\boldsymbol{\delta}}_k = \angle\frac{\boldsymbol{x}(\tau_k)}{x_0(\tau_k)} - \angle \boldsymbol{s}\left(\tilde{\boldsymbol{\theta}}_k\right). \tag{3}$$

In order to evaluate hypothesis $\tilde{\boldsymbol{\delta}}_k$ (computed from path k), it is applied to another path ℓ (which – recall – is assumed to suffer from the same drift). Specifically, $\tilde{\boldsymbol{\delta}}_k$ is used to calibrate for the phase drift of signal ℓ (rearranging (3)):

$$\angle \tilde{\boldsymbol{s}}_k(\tau_\ell) = \angle\frac{\boldsymbol{x}(\tau_\ell)}{x_0(\tau_\ell)} - \tilde{\boldsymbol{\delta}}_k. \tag{4}$$

If $\tilde{\boldsymbol{\delta}}_k$ is the correct hypothesis, then the calibrated phase will be approximately equal (to within the phase noise) to the phase of the path's steering vector, or $\angle \tilde{\boldsymbol{s}}_k(\tau_\ell) \simeq \angle \boldsymbol{s}(\boldsymbol{\theta}_\ell)$. But since $\boldsymbol{\theta}_\ell$ is also unknown (as is $\boldsymbol{\theta}_k$), a set of hypothesized angles $\tilde{\boldsymbol{\theta}}_\ell$ (on the same grid as $\tilde{\boldsymbol{\theta}}_k$) is searched, and the norm of the difference between the two is computed as

$$\epsilon_k\left(\tilde{\boldsymbol{\theta}}_\ell\right) = ||\angle \tilde{\boldsymbol{s}}_k(\tau_\ell) - \angle \boldsymbol{s}\left(\tilde{\boldsymbol{\theta}}_\ell\right)||, \tag{5}$$

generating a grid of norms over $\tilde{\boldsymbol{\theta}}_\ell$. The estimation for $\boldsymbol{\theta}_\ell$ conditioned upon hypothesis $\tilde{\boldsymbol{\delta}}_k$ is the angle $\hat{\boldsymbol{\theta}}_{\ell|k}$ on the grid that yields the minimum norm, or:

$$\hat{\boldsymbol{\theta}}_{\ell|k} = \underset{\tilde{\boldsymbol{\theta}}_\ell}{\operatorname{argmin}}\, \epsilon_k\left(\tilde{\boldsymbol{\theta}}_\ell\right). \tag{6}$$

Note that a grid of norms (computed on grid $\tilde{\boldsymbol{\theta}}_\ell$) is generated for each hypothesis $\tilde{\boldsymbol{\delta}}_k$ (computed on grid $\tilde{\boldsymbol{\theta}}_k$), therefore the search space $(\tilde{\boldsymbol{\theta}}_k, \tilde{\boldsymbol{\theta}}_\ell)$ can be quite large dependent on the grid spacing; however since the data is post-processed after measurement, real-time computation is not an issue.

To mitigate against the noise per path ℓ, the norm in (5) is averaged over all paths $\ell = 1 \ldots K, \ell \neq k$, resulting in the estimated drift per path k as:

$$\hat{\boldsymbol{\delta}}_k = \underset{\tilde{\boldsymbol{\delta}}_k}{\operatorname{argmin}} \left(\frac{1}{K-1} \sum_{\ell=1, \ell \neq k}^{K} \epsilon_k \left(\hat{\boldsymbol{\theta}}_{\ell|k} \right) \right). \tag{7}$$

In the same fashion, the estimated drift per path k is averaged over all paths $k = 1 \ldots K$ when estimating the true bias:

$$\hat{\boldsymbol{\delta}} = \frac{1}{K} \sum_{k=1}^{K} \hat{\boldsymbol{\delta}}_k. \tag{8}$$

With the estimated value of $\hat{\boldsymbol{\delta}}$ in hand, the signal in (1) is calibrated as

$$\hat{\boldsymbol{x}}(\tau_k) = \boldsymbol{x}(\tau_k) \odot e^{-j\hat{\boldsymbol{\delta}}}. \tag{9}$$

Finally, the Maximum Likelihood Estimation (MLE) for $\hat{\boldsymbol{\theta}}_k$ is taken by finding the maximum value over the grid of the MLE projection ratio [47]:

$$\hat{\boldsymbol{\theta}}_k = \underset{\tilde{\boldsymbol{\theta}}_k}{\operatorname{argmax}} \left(\frac{\left| \hat{\boldsymbol{x}}\left(\tau_k\right) \cdot \boldsymbol{s}^H \left(\tilde{\boldsymbol{\theta}}_k \right) \right|}{\left\| \hat{\boldsymbol{x}}\left(\tau_k\right) \right\| \left\| \boldsymbol{s}^H \left(\tilde{\boldsymbol{\theta}}_k \right) \right\|} \right), \tag{10}$$

where H denotes the Hermitian.

III. VIRTUAL PHASED-ARRAY CHANNEL SOUNDER

In order to substantiate the effectiveness of our proposed technique, we applied it to measurements collected with our 60 GHz virtual phased-array channel sounder, which is described in this section.

A. DESCRIPTION OF CHANNEL SOUNDER

Our channel sounder is composed from a T antenna mounted at 1.7 m height on a fixed tripod and an R antenna mounted at 1.7 m height on a 2D positioning table, whose translation plane is parallel to the ground. The T and R antennas have 180° and 360° azimuth beamwidths, respectively, and both have 45° elevation beamwidth. The table forms a virtual planar phased array of 30 × 30 elements at R, so a single measurement consists of $N^T N^R = 900$ ($N^T = 1$, $N^R = 900$) recorded CIRs. The dimensions are comparable to real phased arrays boards fabricated at 60 GHz [32]. (Since there is no T array, only AoA (not AoD) can be estimated.) With half-wavelength ($\lambda/2 = 2.5$ mm) displacement between elements[3], the aperture length is 10.25 cm. The associated steering vector of the system for the R elements indexed through $(u, v) = 0 \ldots 29$ is:

$$\begin{aligned} \boldsymbol{s}(\boldsymbol{\theta}) &= \boldsymbol{s}^R \left(\boldsymbol{\theta}^R \right) \\ &= \left[e^{j\frac{2\pi}{\lambda} \sin\theta^{R,A} \cdot (u \cos\theta^{R,A} + v \sin\theta^{R,E})} \right] \end{aligned}$$

$$= \begin{bmatrix} e^{j\frac{2\pi}{\lambda} \sin\theta^{R,A} \cdot (0 \cdot \cos\theta^{R,A} + 0 \cdot \sin\theta^{R,E})} \\ e^{j\frac{2\pi}{\lambda} \sin\theta^{R,A} \cdot (1 \cdot \cos\theta^{R,A} + 0 \cdot \sin\theta^{R,E})} \\ \vdots \\ e^{j\frac{2\pi}{\lambda} \sin\theta^{R,A} \cdot (29 \cdot \cos\theta^{R,A} + 29 \cdot \sin\theta^{R,E})} \end{bmatrix} \tag{11}$$

[3]The positional error tolerance of the table is 76 μm.

Due to mechanical translation, the scan duration across the 900 elements is 60 minutes. A photograph of the system collecting field measurements in NLoS conditions in a lobby / lecture room environment is shown in Fig. 3.

An arbitrary waveform generator at T synthesizes a pseudorandom (PN) sequence of length 2047 chips and 2 GHz chip rate (0.5 ns delay resolution) modulated by BPSK at IF. The signal is then upconverted to precisely 60.5 GHz and radiated through the antenna. The received signal is downconverted back to IF and sampled into 0.5 ns delay bins. Next, the sampled signal is match filtered with the known PN sequence to generate the CIR. Synchronous triggering of transmission and sampling in untethered mode is implemented through individual Rb clocks on both ends with 1-2 ns/min drift; both ends also have their own local oscillators. The phase noise has a standard deviation of 6.25°. Other details of the system are provided in [14], [31].

B. IDENTIFYING DISTINCT PATHS

Given the aperture length of only 10.25 cm, the received power and delay of a path will vary little across the array. In fact, the respective maximum theoretical variations are 0.3 dB (based on Friis transmission equation) and 0.5 ns (based on the speed of light). Such thresholds can be exploited to identify K distinct paths needed for the calibration technique. There are three reasons for which a sampled peak may not meet the thresholds:

1. There is actually more than one path in the peak, for which small-scale fading could create deep nulls in power or could cause the peak to shift in delay;
2. In dynamic environments, the peak may be obstructed by humans, vehicles, or other moving objects, causing large variation in power and delay;
3. The peak is so weak that its variation is dominated by noise.

In practice, when considering hardware imperfections and noise of our real system, we relaxed the thresholds to 1 dB and 0.5 ns between adjacent elements across the array. The actual variation in the power and delay of the three illustrative paths across the 900 elements is displayed in Fig. 4. Note that for systems such as ours, which have extremely long scan duration, the clock drift was so severe that the peaks corresponding to the same path did not even fall within the same 0.5 ns delay bin across the array. These systems require an additional pre-processing step to align the peaks in delay across the array based on the K distinct paths identified, a step treated in [9], [14], [20], [31], [34].

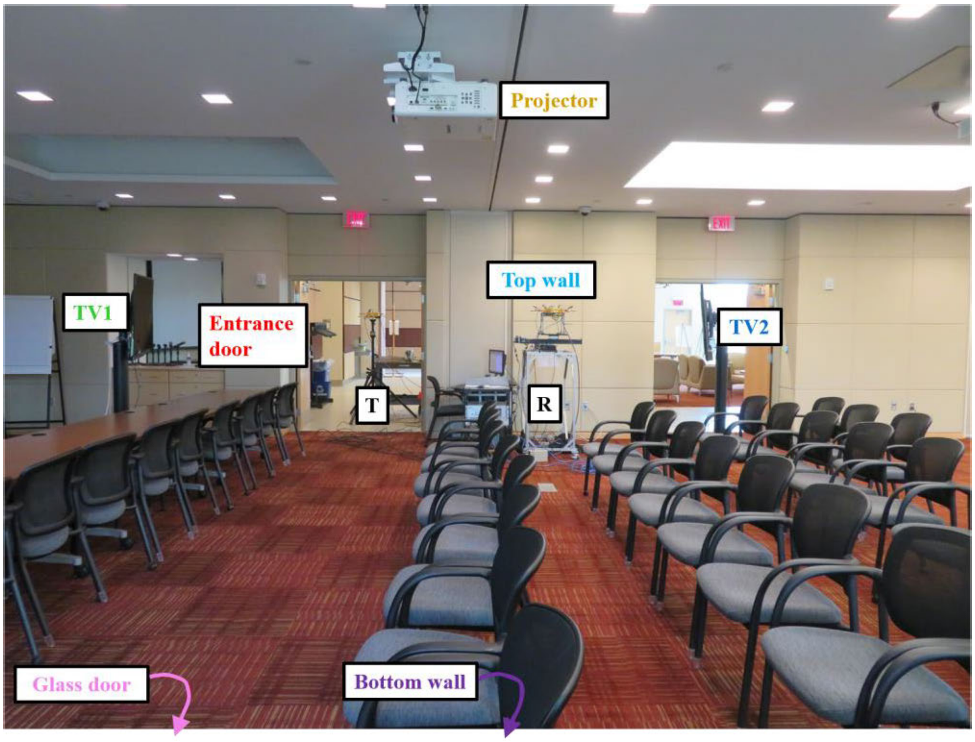

FIGURE 3. Our 60 GHz virtual phased-array channel sounder collecting a channel measurement in NLoS conditions, with the transmitter in the lobby and the receiver in the lecture room.

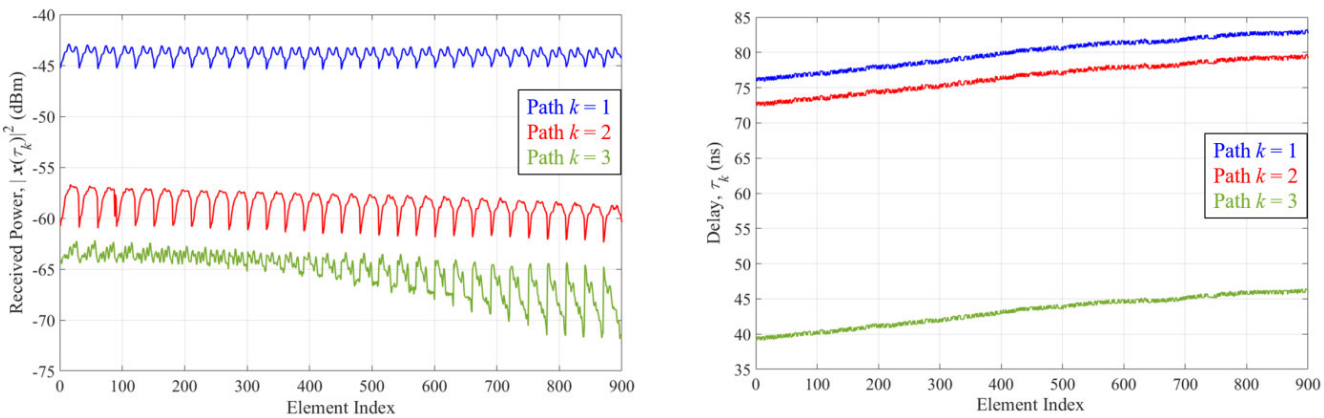

(a) (b)

FIGURE 4. Variation in received power and delay across the 900 elements of our virtual array, for the three illustrative distinct paths ($k = 1, 2, 3$) highlighted in the channel impulse response in Fig. 1.

IV. VERIFICATION

In this section, the calibration technique is verified through our channel sounder. The verification is conducted through two means: The first is based on real measurements collected in both LoS and NLoS conditions; the second is based on simulations in even harsher channel conditions: in lower SNR and with uniformly distributed phase drift, the worst possible case. The last subsection discusses extracting all channel paths – that is – in addition to the distinct paths alone.

A. MEASUREMENT BASED

Real channel measurements were collected for six T-R configurations on our campus in Boulder, Colorado: three in LoS conditions in our laboratory and three in NLoS in a lobby / lecture room. For each configuration, two sequential measurements were collected: The first in (normal) untethered mode, *i.e.* with an individual clock and local oscillator at each end of the sounder as described earlier, for which the system was subject to phase drift; the second measurement was in tethered mode, *i.e.* an optical cable was

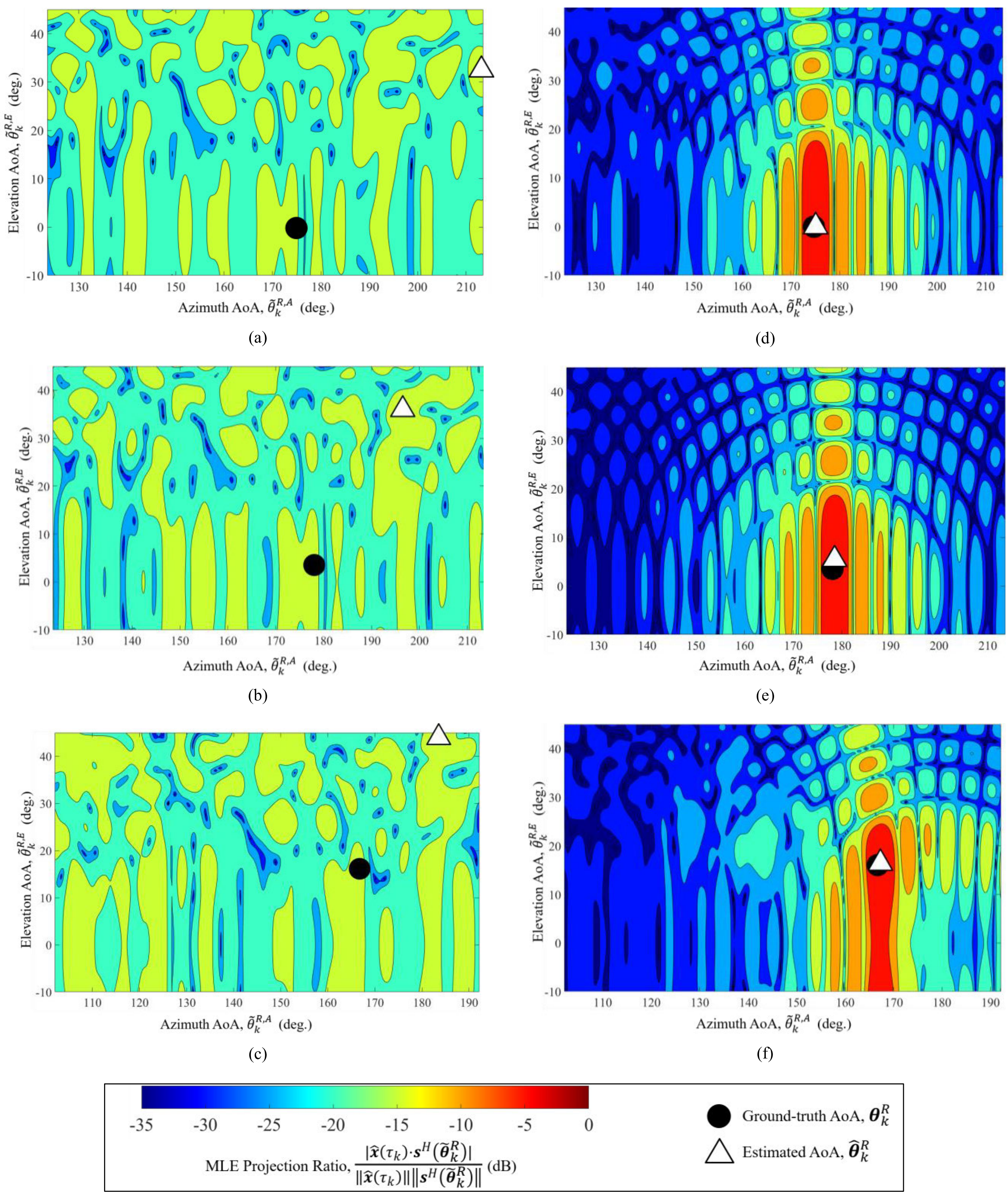

FIGURE 5. MLE projection ratio $\frac{|\hat{x}(\tau_k)\cdot s^H(\tilde{\theta}_k)|}{\|\hat{x}(\tau_k)\|\|s^H(\tilde{\theta}_k)\|}$ (from (10)) for the three illustrative paths highlighted in Fig. 1, before calibration (a) $k = 1$, (b) $k = 2$, (c) $k = 3$ and after calibration (d) $k = 1$, (e) $k = 2$, (f) $k = 3$. After calibration, the characteristic sidelobe pattern of the array steering vector can be observed whereas beforehand the pattern is random. Superimposed on each plot is the ground-truth AoA (θ_k^R) as a black circle and the estimated AoA ($\hat{\theta}_k^R$) as a white triangle.

connected between the T and R for synchronous triggering and for distributing a single local oscillator to eliminate phase drift. The purpose of the second measurement was to provide a ground-truth reference to evaluate performance of the calibration technique. The two sequential measurements were collected in quasi-static conditions, thus with minimum

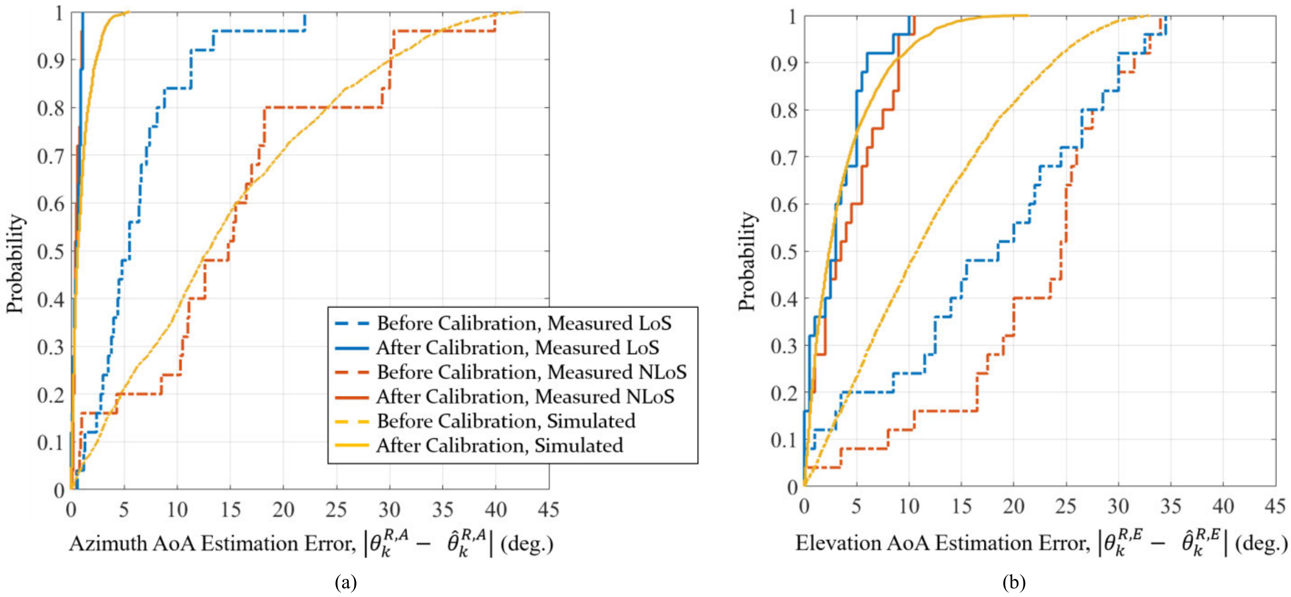

FIGURE 6. Cumulative Distribution Function (CDF) of the AoA estimation error before and after calibration for the real measurements in LoS and NLoS conditions and for the simulations; the AoA error is presented separately for (a) azimuth and (b) elevation.

ambient movement during the 60 minute scan duration each.

Fig. 5 displays the MLE projection ratio ($\frac{|\hat{\boldsymbol{x}}(\tau_k)\cdot \boldsymbol{s}^H(\tilde{\boldsymbol{\theta}}_k)|}{\|\hat{\boldsymbol{x}}(\tau_k)\|\,\|\boldsymbol{s}^H(\tilde{\boldsymbol{\theta}}_k)\|}$ (from (10)) – *before* and *after* calibrating the untethered measurement – for the three distinct paths highlighted in Fig. 1, corresponding to the NLoS configuration pictured in Fig. 3. Clock drift disrupted phase coherence between array elements, so the sidelobes in Fig. 5(a,b,c) for $k = 1, 2, 3$ before calibration appear random, and the estimated AoA $\hat{\boldsymbol{\theta}}_k^R$ (white triangle) is off compared to the ground-truth AoA $\boldsymbol{\theta}_k^R$ (black circle) given from the tethered measurement. Calibration restored phase coherence, for which the sidelobes in Fig. 5(d,e,f) followed the characteristic patterns dictated by the array steering vectors, forming discrete peaks over the grids such that the AoA could be reliably estimated. In fact, after calibration the AoA estimated for all three paths was within 1° of the ground-truth AoA.

In all, there was a total of 50 distinct paths detected over all six T-R configurations – on average 8.33 per configuration – by chance exactly 25 in LoS and exactly 25 in NLoS. The cumulative distribution function (CDF) of the (absolute) error between the estimated and ground-truth AoA per path is shown in Fig. 6(a) for azimuth and in Fig. 6(b) for elevation; in each figure, the CDFs are aggregated separately for the LoS paths (blue) and the NLoS paths (red), as well as for before (dash-dot) and after (solid) calibration. Observe that the azimuth errors after calibration are reduced significantly from before calibration and are all within 1.1°. The average error in LoS and NLoS were 0.54° and 0.52° respectively, hence there was no noticeable difference between the two. The elevation resolution was worse than the azimuth resolution due to the inherent structure of the array lying completely in the azimuth plane [11]. This can be observed in Fig. 5(d,e,f) through the wider lobes in elevation compared to azimuth. That is why the average elevation errors of 3.06° and 4.12° in LoS and NLoS respectively were much larger than the azimuth errors.

Although the tethered measurements are referred to as ''ground-truth'' because they did not suffer from phase drift, they were still subject to phase noise and finite angular resolution, hence to AoA estimation error. So the errors in Fig. 6 do not represent the error in the phase calibration technique per se, but rather the difference in the estimated AoA between the untethered and tethered measurements. In order to get a better handle on the residual error after calibration itself, simulations with genuine ground-truth (zero error) are necessary and accordingly were run the following section.

B. SIMULATION BASED

The simulated-based verification adhered to the methodology proposed in [1] for benchmarking RF channel sounders, in which the channel sounder is represented mathematically through a system model. The model parameters were the actual PN sequence used as a probing signal distorted by the RF front ends of the T and R characterized through the back-to-back method [14]. The T and R antenna patterns were characterized in an anechoic chamber, amongst others system-specific parameters not mentioned here, to ensure accurate representation. The system model was applied to a synthetic channel composed from 100 ground-truth paths with known properties. The output of the system model was 900 CIRs across the array, equivalent to what the channel sounder would actually measure in the field. Per CIR, a random phase was drawn from a uniform distribution (corresponding to the most severe case of phase drift) and added

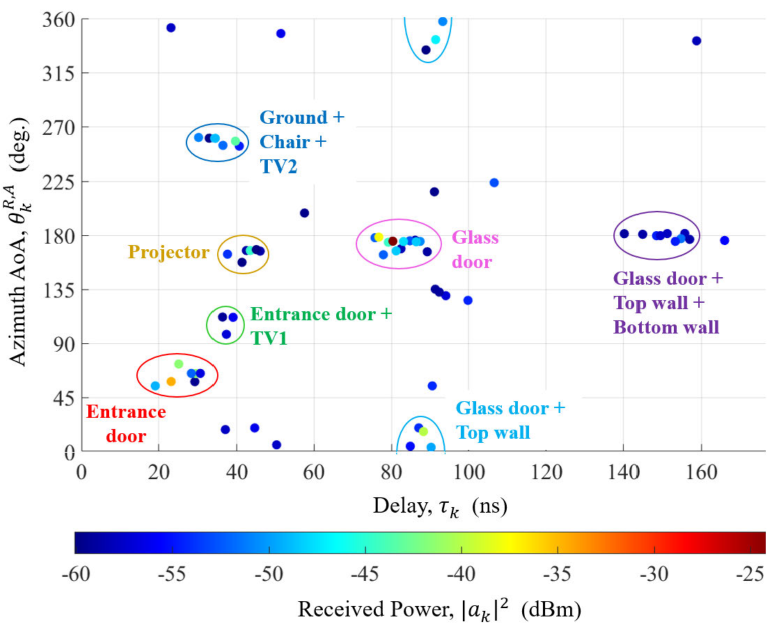

(a)

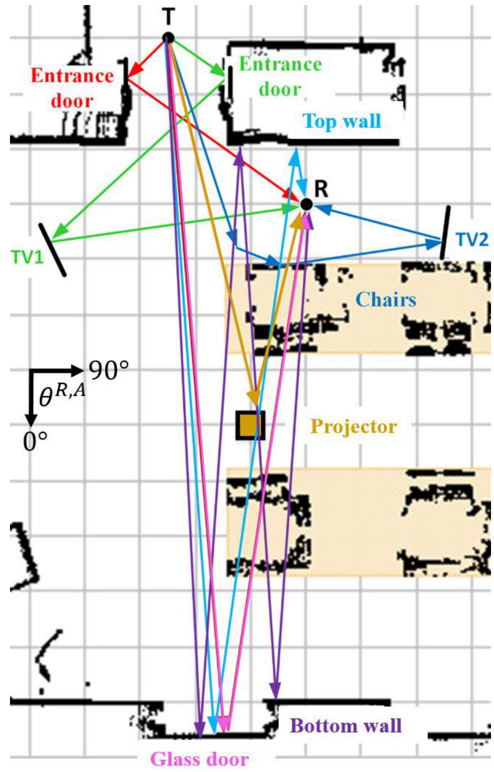

(b)

FIGURE 7. All (distinct and indistinct) paths extracted from the NLoS meaurement in the lobby / lecture room from Fig. 3. (a) The 71 paths are plotted in azimuth AoA vs. delay and their received power coded against the color bar; diffuse paths are clustered with seven strong specular paths that were identified; the clusters are circled and labeled according to the specular paths. (b) The seven specular paths are raytraced in the enviorment map, corresponding to the view in Fig. 3; the azimuth AoA coordinate system is shown in reference to Fig. 7(a).

to the phase of the samples; also added to the samples was thermal noise.

The phase drift was then estimated through the calibration technique from the eight strongest paths (to mimic the real measurements), whose SNR varied up to 20 dB (whereas for the real measurements they were all above 20 dB), and their AoAs were estimated. The process was repeated for a total of 50 synthetic channels. Fig. 6 also includes the CDF of the AoA errors before (dash-dot) and after calibration (solid) for the simulated data (orange). The calibration technique was able to achieve performance comparable to the real measurements, with average errors of 0.60° and 2.39° in azimuth and elevation, respectively. In fact, the simulated elevation error was considerably lower than the measurements errors despite the harsher channel conditions, most likely stemming from that fact that in the simulations the ground-truth references genuinely had zero error (in contrast to the ground-truth reference from the tethered measurements).

C. INDISTINCT PATHS

Although the paths used for calibration must be distinct (per definition in Section III.B), in reality there will be many other paths that are either non-stationary across the array, combined with other paths in the same delay bin, or weak and thus more susceptible to noise. These *indistinct* paths nevertheless suffer from the same phase drift as the distinct paths and so the phase drift estimated from calibration can be applied to estimate their properties as well.

Fig. 7(a) displays all paths extracted from the illustrative measurement in NLoS shown in Fig. 3. The paths are plotted in azimuth AoA vs. delay only (since the elevation AoA was between 0°–10° for most paths given that the T and R were at the same height) and their received power against the color bar. In addition to the nine distinct paths, there were 62 indistinct paths, for a total of 71. As is consistent with results reported in other papers [49], [50], weaker diffuse paths clustered around stronger specular paths that could be clearly identified as reflecting from ambient objects. Those clusters are labeled according to the specular paths. Using their delay, azimuth, and elevation, the seven specular paths were raytraced back to the map of the environment, as shown in Fig. 7(b); the raytraced paths are colored according to the labeled clusters. Note that some paths went unclustered, originating from unidentified objects in the room.

V. CONCLUSIONS

Phase drift is inherent to radio-frequency channel sounders that operate in untethered mode, due to separate transmitter and receiver clocks. While tolerable at microwave frequencies, at millimeter-wave the drift between even the best Rubidium clocks can translate into a full cycle of phase drift during a complete scan over an antenna array, disrupting the phase coherence essential for angle estimation. The severe phase drift stems from both shorter wavelength and from longer scans by virtue of more array elements. Existing techniques to calibrate for phase bias due to hardware imperfections either require a reference signal or a good initial estimate for the bias, which in general cannot be assumed for bias resulting from phase drift, given its dynamic and spiky behavior over time. As such, this paper describes a blind calibration technique that can even deal with phase drift that occurs during long scan durations. The robustness of the technique was substantiated both through real measurements with our virtual-array channel sounder in non-line-of-sight conditions, and through simulations with the worse possible case of phase drift (uniformly distributed) and in low signal-to-noise conditions.

ACKNOWLEDGMENT

Publication of the United States government, not subject to copyright in the U.S.

REFERENCES

[1] C. Gentile *et al.*, "Methodology for benchmarking radio-frequency channel sounders throught a system model," *IEEE Trans. Wireless Commun.*, to be published.
[2] A. Maltsev, R. Maslennikov, A. Sevastyanov, A. Khoryaev, and A. Lomayev, "Experimental investigations of 60 GHz WLAN systems in office environment," *IEEE J. Sel. Areas Commun.*, vol. 27, no. 8, pp. 1488–1499, Oct. 2009.
[3] H. Sawada, H. Nakase, S. Kato, M. Umehira, K. Sato, and H. Harada, "Impulse response model and parameters for indoor channel modeling at 60 GHz," in *Proc. IEEE 71st Veh. Technol. Conf.*, May 2010, pp. 1–5.
[4] S. Hur, Y.-J. Cho, J. Lee, N.-G. Kang, J. Park, and H. Benn, "Synchronous channel sounder using horn antenna and indoor measurements on 28 GHz," in *Proc. IEEE Int. Black Sea Conf. Commun. Netw. (BlackSeaCom)*, May 2014, pp. 83–87.
[5] M. R. Akdeniz, Y. Liu, M. K. Samimi, S. Sun, S. Rangan, T. S. Rappaport, and E. Erkip, "Millimeter wave channel modeling and cellular capacity evaluation," *IEEE J. Sel. Areas Commun.*, vol. 32, no. 6, pp. 1164–1179, Jun. 2014.
[6] R. Muller, S. Hafner, D. Dupleich, R. S. Thoma, G. Steinbock, J. Luo, E. Schulz, X.'Lu, and G. Wang, "Simultaneous multi-band channel sounding at mm-Wave frequencies," in *Proc. 10th Eur. Conf. Antennas Propag. (EuCAP)*, Davos, Switzerland, Apr. 2016, pp. 1–5.
[7] J.-J. Park, J. Liang, J. Lee, H.-K. Kwon, M.-D. Kim, and B. Park, "Millimeter-wave channel model parameters for urban microcellular environment based on 28 and 38 GHz measurements," in *Proc. IEEE 27th Annu. Int. Symp. Pers., Indoor, Mobile Radio Commun. (PIMRC)*, Sep. 2016, pp. 1–5.
[8] B. N. Liya and D. G. Michelson, "Characterization of multipath persistence in device-to-device scenarios at 30 GHz," in *Proc. IEEE Globecom Workshops (GC Wkshps)*, Dec. 2016, pp. 1–6.
[9] G. R. MacCartney and T. S. Rappaport, "A flexible millimeter-wave channel sounder with absolute timing," *IEEE J. Sel. Areas Commun.*, vol. 35, no. 6, pp. 1402–1418, Jun. 2017.
[10] W. Khawaja, O. Ozdemir, Y. Yapici, I. Guvenc, and Y. Kakishima, "Coverage enhancement for mm Wave communications using passive reflector," in *Proc. IEEE Global Symp. Millim. Waves (GSMM)*, Boulder, CO, USA, May 2018, pp. 1–6.
[11] A. W. Mbugua, W. Fan, Y. Ji, and G. F. Pedersen, "Millimeter wave multi-user performance evaluation based on measured channels with virtual antenna array channel sounder," *IEEE Access*, vol. 6, pp. 12318–12326, Mar. 2018.
[12] A. W. Mbugua, W. Fan, K. Olesen, X. Cai, and G. F. Pedersen, "Phase compensated optical fiber based ultra-wideband channel sounder," *IEEE Trans. Microw. Theory Techn.*, vol. 68, no. 2, pp. 636–647, Nov. 2019.
[13] A. J. Weiss, J. Quimby, R. Leonhardt, B. Jamroz, D. Williams, K. Remley, P. Vouras, and A. Elsherbeni, "Setup and control of a mmWave synthetic aperture measurement system with uncertainties," in *Proc. 94th ARFTG Microw. Meas. Conf.*, San Antonio, TX, USA, Jan. 2020, pp. 1–4.
[14] R. Sun, P. B. Papazian, J. Senic, Y. Lo, J.-K. Choi, K. A. Remley, and C. Gentile, "Design and calibration of a double-directional 60 GHz channel sounder for multipath component tracking," in *Proc. 11th Eur. Conf. Antennas Propag. (EuCAP)*, Paris, France, Mar. 2017, pp. 3336–3340.
[15] Z. Wen, H. Kong, Q. Wang, S. Li, X. Zhao, M. Wang, and S. Sun, "mmWave channel sounder based on COTS instruments for 5G and indoor channel measurement," in *Proc. IEEE Wireless Commun. Netw. Conf.*, Apr. 2016, pp. 1–7.
[16] S. Salous, S. M. Feeney, X. Raimundo, and A. A. Cheema, "Wideband MIMO channel sounder for radio measurements in the 60 GHz band," *IEEE Trans. Wireless Commun.*, vol. 15, no. 4, pp. 2825–2832, Apr. 2016.
[17] R. J. Weiler, W. Keusgen, A. Maltsev, T. Kuhne, A. Pudeyev, L. Xian, J. Kim, and M. Peter, "Millimeter-wave outdoor access shadowing mitigation using beamforming arrays," in *Proc. 10th Eur. Conf. Antennas Propag. (EuCAP)*, Davos, Switzerland, Apr. 2016, pp. 1–5.
[18] C. U. Bas, R. Wang, S. Sangodoyin, S. Hur, K. Whang, J. Park, J. Zhang, and A. F. Molisch, "Dynamic double directional propagation channel measurements at 28 GHz–Invited paper," in *Proc. IEEE 87th Veh. Technol. Conf. (VTC Spring)*, Jun. 2018, pp. 1–6.
[19] C. Slezak, V. Semkin, S. Andreev, Y. Koucheryavy, and S. Rangan, "Empirical effects of dynamic human-body blockage in 60 GHz communications," *IEEE Commun. Mag.*, vol. 56, no. 12, pp. 60–66, Dec. 2018.
[20] D. Caudill, P. B. Papazian, C. Gentile, J. Chuang, and N. Golmie, "Omnidirectional Channel Sounder With Phased-ArrayAntennas for 5G Mobile Communications," *IEEE Trans. Microw. Theory Techn.*, vol. 67, no. 7, pp. 2936–2945, Jul. 2019.
[21] *Terragraph by Facebook, Solving the Urban Bandwidth Challenge*. Accessed: Jun. 2020. [Online]. Available: https://www.terragraph.com
[22] M. Steinbauer, A. F. Molisch, and E. Bonek, "The double-directional radio channel," *IEEE Antennas Propag. Mag.*, vol. 43, no. 4, pp. 51–63, Aug. 2001.
[23] J. Högbom, "Aperture synthesis with a non-regular distribution of interferometer baselines," *Astrophys. J. Suppl.*, vol. 15, pp. 417–426, Jun. 1974.
[24] R. Schmidt, "Multiple emitter location and signal parameter estimation," *IEEE Trans. Antennas Propag.*, vol. 34, no. 3, pp. 276–280, Mar. 1986.
[25] R. Roy and T. Kailath, "ESPRIT-estimation of signal parameters via rotational invariance techniques," *IEEE Trans. Acoust., Speech, Signal Process.*, vol. 37, no. 7, pp. 984–995, Jul. 1989.
[26] J. A. Fessler and A. O. Hero, "Space-alternating generalized expectation-maximization algorithm," *IEEE Trans. Signal Process.*, vol. 42, no. 10, pp. 2664–2677, Oct. 1994.
[27] A. Richter, "Estimation of radio channel parameters: Models and algorithms," Ph.D. dissertation, Dept. Elect. Eng. Inf. Technol., Technische Universität Ilmenau, Ilmenau, Germany, 2005.
[28] M. Atif Yaqoob, F. Tufvesson, A. Mannesson, and B. Bernhardsson, "Direction of arrival estimation with arbitrary virtual antenna arrays using low cost inertial measurement units," in *Proc. IEEE Int. Conf. Commun. Workshops (ICC)*, Budapest, Hungary, Jun. 2013, pp. 79–83.
[29] A. Badawy, T. Khattab, D. Trinchero, T. El Fouly, and A. Mohamed, "A simple AoA estimation scheme," 2014, *arXiv:1409.5744*. [Online]. Available: http://arxiv.org/abs/1409.5744
[30] A. Mannesson, M. Atif Yaqoob, B. Bernhardsson, and F. Tufvesson, "Tightly coupled positioning and multipath radio channel tracking," *IEEE Trans. Aerosp. Electron. Syst.*, vol. 52, no. 4, pp. 1522–1535, Aug. 2016.
[31] P. B. Papazian, J. K. Choi, J. Senic, P. Jeavons, C. Gentile, N. Golmie, R. Sun, D. Novotny, and K. A. Remley, "Calibration of millimeter-wave channel sounders for super-resolution multipath component extraction," in *Proc. 10th Eur. Conf. Antennas Propag. (EuCAP)*, Davos, Switzerland, Apr. 2016, pp. 1–5.
[32] B. Rupakula, A. Nafe, S. Zihir, Y. Wang, T.-W. Lin, and G. Rebeiz, "63.5–65.5-GHz Transmit/Receive phased-array communication link with 0.5–2 Gb/s at 100–800 m and ±50° scan angles," *IEEE Trans. Microw. Theory Techn.*, vol. 66, no. 9, pp. 4108–4120, Sep. 2018.
[33] D. Ferreira, R. F. S. Caldeirinha, and N. Leonor, "Real-time high-resolution radio frequency channel sounder based on the sliding correlation principle," *IET Microw., Antennas Propag.*, vol. 9, no. 8, pp. 837–846, Jun. 2015.

[34] Y.-Q. Lin, W. C. Cheng, T. H. Liu, Y. R. Chen, W.-H. Sheen, and Z.-M. Tsai, "Accurate synchronization method of 38-GHz 5G channel measurement system," in *Proc. 47th Eur. Microw. Conf. (EuMC)*, Oct. 2017, pp. 747–750.
[35] J. Pierre and M. Kaveh, "Experimental performance of calibration and direction-finding algorithms," in *Proc. Int. Conf. Acoust., Speech, Signal Process. (ICASSP)*, Apr. 1991, pp. 1365–1368.
[36] C. M. S. See, "Sensor array calibration in the presence of mutual coupling and unknown sensor gains and phases," *Electron. Lett.*, vol. 30, no. 5, pp. 373–374, Mar. 1994.
[37] Q. Huang, H. Zhou, J. Bao, and X. Shi, "Mutual coupling calibration for microstrip antenna arrays via element pattern reconstruction method," *IEEE Antennas Wireless Propag. Lett.*, vol. 13, pp. 51–54, Dec. 2014.
[38] A. Paulraj and T. Kailath, "Direction of arrival estimation by eigenstructure methods with unknown sensor gain and phase," in *Proc. IEEE Int. Conf. Acoust., Speech, Signal Process. (ICASSP)*, vol. 10, Apr. 1985, pp. 640–643.
[39] G. C. Brown, J. H. McClellan, and E. J. Holder, "A phased array calibration technique using eigenstructure methods," in *Proc. IEEE Int. Conf. Radar*, May 1990, pp. 304–308.
[40] B. Friedlander and A. J. Weiss, "Eigenstructure methods for direction finding with sensor gain and phase uncertainties," in *Proc. Int. Conf. Acoust., Speech, Signal Process. (ICASSP)*, Apr. 1988, pp. 2681–2684.
[41] B. Friedlander and A. J. Weiss, "Direction finding in the presence of mutual coupling," *IEEE Trans. Antennas Propag.*, vol. 39, no. 3, pp. 273–284, Mar. 1991.
[42] A. Khallaayoun, R. J. Weber, and Y. Huang, "A blind iterative calibration method for high resolution DOA estimation," in *Proc. Military Commun. Conf.*, Nov. 2011, pp. 199–204.
[43] M. Z. Ikram, M. Ali, and D. Wang, "Joint antenna-array calibration and direction of arrival estimation for automotive radars," in *Proc. IEEE Radar Conf. (RadarConf)*, May 2016, pp. 1–5.
[44] L. Liu and Y. Wu, "Direction of arrival estimation by convex optimization methods with unknown sensor gain and phase," *IEEE Access*, vol. 6, pp. 65367–65375, 2018.
[45] X. Wei, Y. Jiang, and X. Wang, "Calibration of phase shifter network for hybrid beamforming in mmWave massive MIMO systems," in *Proc. IEEE Int. Conf. Commun. (ICC)*, Shanghai, China, May 2019, pp. 2302–2315.
[46] F. Quitin, P. De Doncker, F. Horlin, and W. P. Tay, "Virtual multi-antenna array for estimating the direction of a transmitter: System, bounds, and experimental results," *IEEE Trans. Veh. Technol.*, vol. 67, no. 2, pp. 1510–1520, Feb. 2018.
[47] I. Ziskind and M. Wax, "Maximum likelihood localization of multiple sources by alternating projection," *IEEE Trans. Acoust., Speech, Signal Process.*, vol. 36, no. 10, pp. 1553–1560, Oct. 1988.
[48] K. Hausmair, K. Witrisal, P. Meissner, C. Steiner, and G. Kail, "SAGE algorithm for UWB channel parameter estimation," in *Proc. COST Manage. Committee Meeting*, Athens, Greece, Feb. 2010, pp. 1–7.
[49] C. Gentile, P. B. Papazian, R. Sun, J. Senic, and J. Wang, "Quasi-deterministic channel model parameters for a data center at 60 GHz," *IEEE Antennas Wireless Propag. Lett.*, vol. 17, no. 5, pp. 808–812, May 2018.
[50] C. Lai, R. Sun, C. Gentile, P. B. Papazian, J. Wang, and J. Senic, "Methodology for multipath-component tracking in millimeter-wave channel modeling," *IEEE Trans. Antennas Propag.*, vol. 67, no. 3, pp. 1826–1836, Mar. 2019.

JACK CHUANG received the Ph.D. degree from Pennsylvania State University, in 2008. He was a Graduate Research Assistant with the Communications and Space Sciences Laboratory (CSSL), Pennsylvania State University. He then worked at BAE Systems in electronic warfare and Cisco Systems in spectrum sharing. He is currently with the Communication Technology Laboratory, NIST, Gaithersburg, MD, USA, developing 5G mmWave channel sounders.

JELENA SENIC received the B.S. and M.S. degrees in electrical engineering from the Faculty of Electrical Engineering, University of Belgrade, Serbia, in 2009 and 2010, respectively. Since January 2015, she has been a Researcher with NIST. Her current research interests include millimeter-wave communications, measurements of signal propagation, and channel modeling for 5G. The team in which she works received the Best Measurement Paper Award at the EuCAP 2017.

CHUNMEI LIU received the Ph.D. degree in computer systems from the Massachusetts Institute of Technology (MIT), in 2005. She is currently working as a Researcher with the Wireless Networks Division, National Institute of Standards and Technology (NIST). She has been continually working in the areas of wireless communications and networking, since 2005. Her current research interests include public safety communications in cellular networks and machine learning.

CAMILLO GENTILE (Member, IEEE) received the Ph.D. degree in electrical engineering from Pennsylvania State University, in 2001, with a dissertation on computer vision and artificial intelligence. He joined the National Institute of Standards and Technology, Gaithersburg, MD, USA, in 2001, where he is currently the Project Leader with the Communications Technology Laboratory, Wireless Networks Division. He has authored over 80 peer-reviewed journal and conference papers and a book on geolocation techniques and millimeter-wave channel modeling. His current research interests include channel modeling and physical-layer modeling for 5G communications systems.

SUNG YUN JUN (Member, IEEE) received the Ph.D. degree in electronic engineering from the University of Kent, U.K., in 2018. Since 2018, he has been a Postdoctoral Associate with the RF Technology Division, National Institute of Standards and Technology, Boulder, CO, USA. His current research interests include antennas, microwave devices, and channel measurements and modeling of radio propagation.

DEREK CAUDILL received the B.S. degree in electrical engineering and the M.S. degree in electrical and computer engineering from the University of Massachusetts Amherst, in 2016 and 2017, respectively. As a Researcher within the Communications Technology Laboratory, NIST, he supports the data acquisition efforts of mmWave channel model measurements and the systems that such measurements depend on.